Structural disorder-driven topological phase transition in noncentrosymmetric BiTeI

Paul Corbae, Frances Hellman, and Sinéad M. Griffin

Phys. Rev. B **103**, 214203 — Published 21 June 2021

DOI: 10.1103/PhysRevB.103.214203

Structural disorder-driven topological phase transition in noncentrosymmetric BiTeI

Paul Corbae,[1,3] Frances Hellman[1,2,3] and Sinéad M. Griffin,[3,4]
[1]Department of Materials Science, University of California, Berkeley, California, 94720, USA
[2]Department of Physics, University of California, Berkeley, California, 94720, USA
[3]Materials Science Division, Lawrence Berkeley National Laboratory, Berkeley, California, 94720, USA
[4] Molecular Foundry, Lawrence Berkeley National Laboratory, Berkeley, California, 94720, USA
*To whom correspondence should be addressed; E-mail: pcorbae@berkeley.edu.
(Dated: May 13, 2021)

We investigate using local structural disorder to induce a topologically nontrivial phase in a solid state system. Using first-principles calculations, we introduce structural disorder in the trivial insulator BiTeI and observe the emergence of a topological insulating phase. By modifying the bonding environments, the crystal-field splitting is enhanced, with spin-orbit interactions producing a band inversion in the bulk electronic structure. Analysis of the Wannier charge centers and the surface electronic structure reveals a strong topological insulator with Dirac surface states. Finally, we propose a prescription for inducing topological states from disorder in crystalline materials. Understanding how local environments produce topological phases is a key step for predicting disordered and amorphous topological materials.

The discovery of nontrivial topological phases in materials has been at the forefront of condensed matter physics for both their fundamental importance and their potential in applications ranging from low-power electronics to quantum computing. High-throughput searches and classification schemes for topological materials exploit crystalline symmetries, and how these symmetries determine band connectivity [1–7]. Such symmetry indicators have enabled the prediction of thousands of crystalline topological materials. However, materials without intrinsic or long-range crystalline symmetries, such as amorphous and quasicrystalline materials [8, 9], have no such classification scheme. Nonetheless, evidence for topological surface states has been experimentally and theoretically observed in an amorphous topologically insulating system [10, 11]. Recently, Marsal et al., [12] exploited local environments to compute the topological phase diagram in a coordinated amorphous structure. These works find that local interactions and connectivity determine the relevant features in the electronic structure to produce topological phases, and emphasize the importance of local chemical environments in topological materials. Understanding how structural disorder contributes to and enhances topological phases will drive predictions of disordered and amorphous topological materials based on local structural properties.

Small gap semiconductors with strong spin-orbit interactions (SOI) are ideal systems to probe how local environments affect the band topology. In such systems, a band inversion and a topological phase can be induced by tuning the chemical environment to modify the crystal-field splitting (CFS) [13]. Systems with a strong SOI and no inversion are subject to Rashba spin-splitting: without I-symmetry, the degeneracy between $\psi_{-k,\uparrow}$ and $\psi_{k,\uparrow}$ is lifted so that the bands split at non-specific k-points, and a resulting band inversion can occur away from Γ in the Brillouin zone (BZ). If the states near the Fermi level are of the same orbital character and also close in energy, they can couple together effectively through a Rashba Hamiltonian, further reducing the band gap at relevant points in the BZ [14].

Several routes to inducing topological phase transitions (TPTs) from normal to topological insulator (TI) have been proposed in solid-state systems, including using temperature[15, 16], pressure [17] and strain [18]. Topological Anderson insulators are an example where onsite disorder pushes a trivial insulator through a gapless state into a topologically nontrivial state [19, 20]. Typically, Anderson models incorporate an onsite disorder term which can be applied to non-crystalline solids [21], however here we incorporate disorder with perturbations to the atomic positions. No studies to date have looked at the effect of this random structural disorder on the topological character.

In this work, we study how local structural disorder affects the CFS and SOI in the small-gap semiconductor BiTeI and identify the structural motifs that play a crucial role in producing the nontrivial band topology. First, we present our scheme for introducing structural disorder in BiTeI and analyze the subsequent charge redistribution upon symmetry breaking. Using first-principles calculations we show that, as bond lengths change, the CFS is enhanced leading to a bandgap reduction. We observe a TPT from trivial insulator to Weyl semimetal to TI originating from a bulk band inversion when spin-orbit coupling (SOC) is included. These topological phases emerge in a crystalline material with reduced crystalline symmetries. We confirm the TPT by studying the surface state spectrum and calculating topological invariants from Wannier charge centers, observing a Dirac cone on the surface resulting from a strong $\mathbb{Z}_2$ index. This work provides a pathway to understanding local chemical environments in topological materials and their extension to amorphous systems by using disorder in crystalline systems to elucidate the physical origin of the TPT, prompting a route for materials discovery [10].

BiTeI is a trigonal, noncentrosymmetric material adopting the $P3m1$ space group (No. 156). The primi-

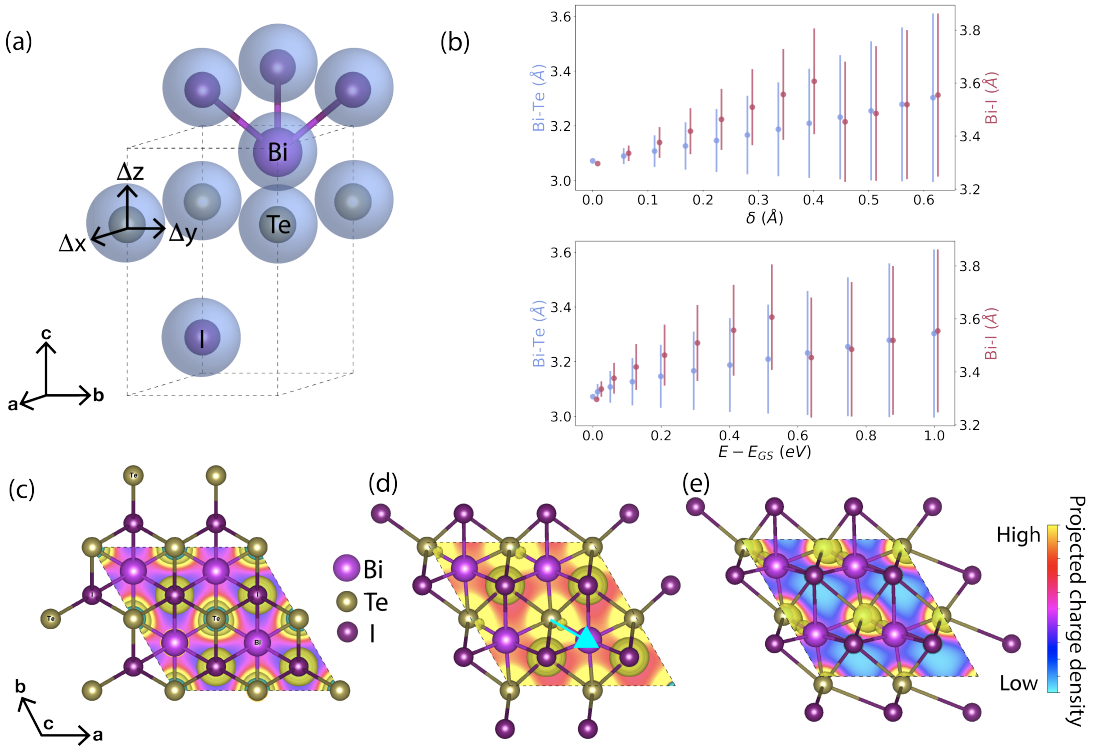

FIG. 1. **Structural disorder induced charge redistribution**. (a) BiTeI primitive unit cell. Blue spheres represent the allowed random displacements Δx, Δy, and Δz. (b) Bi-Te and Bi-I bond lengths vs. disorder/energy per unit cell. The Bi-Te bonds shift to a higher mean length and develop a larger σ. The important bond for the TPT, Bi-Te = 2.9 Å, can be seen developing around 0.4 Å. The Bi-I bonds initially develops a higher mean length with large σ and then drops around 3.50 Å with low σ after the TPT. (c-e) Partial charge density of the (001) plane for bands near the Fermi level in structures with d_{av}=0.00 Å, d_{av}=0.28 Å, and d_{av}=0.56 Å, respectively. As the structures become more disordered the charge density distorts into the y-direction (indicated by the blue arrow in (d)) and the charge moves to the Bi-Te bond.

tive unit cell contains a single Bi, Te, and I configured in layers of triangular networks along the c-axis (Fig. 1(a)), resulting in a C_{3v} rotational symmetry about the c-axis. The Te-Bi-I network forms a trigonal prism surrounding the Bi atoms, which are separated by a van der Waals gap. In this undisordered structure the equilibrium Bi-Te bond length is 3.07 Å and the Bi-I bond length is 3.29 Å, bond lengths in the PBE framework are typically within 1−2% (experimental values are 3.04 Å and 3.27 Å respectively). This structure is a trivial insulator with an experimental bandgap of 0.36 eV [22]. To understand how topology is influenced by the local chemical environment we generated disordered structures as follows: We pull a random number from a uniform distribution between −0.15 Å and 0.15 Å and add it to each Wyckoff position in the unit cell for each direction. This generated a disordered structure with an average atomic displacement d_{av}=0.62 Å per unit cell, similar in value to the change in interatomic spacing between the crystalline and amorphous phases of Bi_2Se_3 in experiment[10]. From this disordered structure, we created interpolated snapshots between the undisordered and fully disordered crystal with d_{av}=0.62 Å to track the electronic and topological properties with increasing disorder. The final structure is in the $P1$ space group after the C_{3v} and remaining symmetry elements are removed by the structural disorder.

Fig. 1(b) shows the distributions (mean bond lengths with bars representing the standard deviation) for Bi-Te and Bi-I bond lengths for our disordered structures as a function of average displacement and energy difference from the ground state. We see that with increasing disorder, the distribution of Bi-Te bond lengths develops a larger standard deviation while the mean bond length becomes larger. The smaller Bi-Te bonds shift to a value of 2.9 Å – this Bi-Te bond plays an important role in the TPT as discussed later. Additionally, the distribution of Bi-I bond lengths spread out with large deviation and then moves to 3.5 Å with lower deviation.

The Bi-Te bond shortening and Bi-I bond lengthening has important implications on the charge density. Fig. 1(c) plots the charge density of bands at the Fermi level near the A point which are involved in the TPT for the undisordered crystal. We also plot the charge density for the bands projected onto the (001) plane depicting the C_{3v} symmetry and the charge sitting on the Te and I atoms. As we disorder crystalline BiTeI, Fig. 1(d-e), the charge density moves from being centered on the Te and I ions to the Bi-Te bond. This is important because,

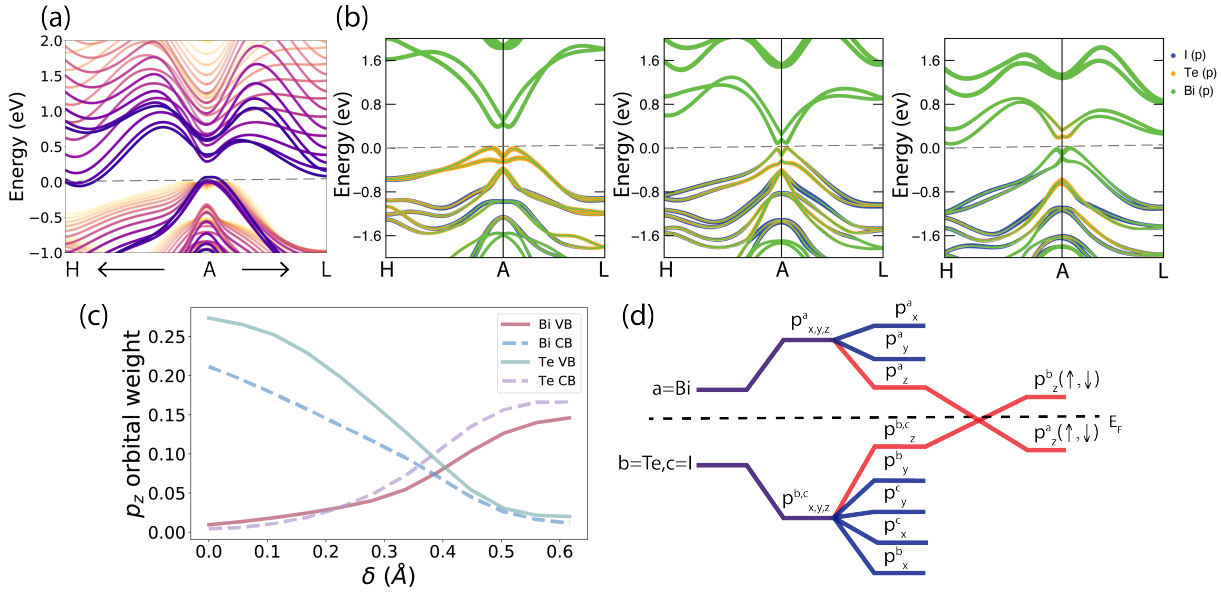

FIG. 2. **Bulk electronic bandstructure**. (a) Bulk bandstructure in the $H-A-L$ direction without SOC. Structural disorder modifies the CFS pushing bands near the Fermi level closer and reducing the energy gap. Darker colors represent more disordered structures. (b) The bandstructure with SOC for d_{av}=0.00 Å, d_{av}=0.28 Å, and d_{av}=0.45 Å, respectively. The Bi weight in green moves from the CB to VB and vice versa for Te in orange. (c) The Bi/Te p_z orbital weight at A as a function of average atomic displacement. With increasing displacement the Bi and Te weight of the VB (CB) switch around 0.4 Å. (d) Energy level splitting diagram for disordered BiTeI after the TPT. The three splittings represent chemical bonding, crystal field, and SOC. By breaking the C_{3v} symmetry the $p_{x,y}$ orbitals are no longer degenerate.

as we will describe later, the TPT band inversion occurs between the Bi and Te p orbitals near the Fermi level. The charge density is redistributed in the y-direction due to the increased p_y orbital presence at the Fermi level. This increase is attributed to the shortening of the Bi-Te bonds, which happens primarily in the y-direction. The y-direction is not specific, rather the important feature is a shortening of the Bi-Te bond and the subsequent charge redistribution. In summary, in our disordered BiTeI, the Bi-Te bond gets shorter causing a charge redistribution along the Bi-Te bond, resulting in a broken 3-fold rotation symmetry and a new crystal-field environment for the states near the Fermi level.

Next, we examine the influence of the structural changes on the electronic and topological properties of disordered BiTeI. Full DFT calculation details are given in the supplemental materials [23](see, also, references [24–31] therein). The calculated electronic structure is shown in Fig. 2 with and without SOC included to disentangle how crystal-field effects and SOC change with atomic displacement. Due to the lack of a center of inversion, we examine the states along the $H-A-L$ direction to track topological band inversion. Fig. 2(a) shows the calculated electronic bandstructure for increasing values of d_{av} without SOC. We find that for increasing d_{av}, the resulting changes in the CFS at A reduces the band gap and pushes the bands at the Fermi level closer together. This large crystal-field enhancement is a result of the lifting of the degeneracy between the p_x and p_y orbitals upon displacement when the three-fold rotational symmetry is broken. This causes an increased p_y orbital contribution near the Fermi level, seen in the partial charge density. The orbital overlap produces large splitting pushing states near the Fermi level closer together as shown in Fig. 1(e) and Fig. 2(a).

To understand the role of SOC on the disordered electronic structure, Fig. 2(b) plots the bandstructure for d_{av} = 0.0 Å, d_{av} = 0.3 Å, and d_{av} = 0.5 Å, respectively, with SOC included. SOC breaks the spin degeneracy giving rise to splitting at positions in the Brillouin zone away from high-symmetry points and causes a large Rashba spin-splitting near the Fermi level in all structures [32]. Importantly, by incorporating SOC we observe a reduction of the bandgap, and, with increasing d_{av}, a band inversion occurs at the A point. This band inversion produces the TPT in disordered BiTeI. The origin of the band inversion can be understood by considering the p-orbital projections of Bi, Te, and I onto the bandstructure. Initially the Te (orange) and I (blue) weight is concentrated in the valence band (VB) and the Bi weight (green) in the conduction band (CB). After the transition the Bi weight is in the VB and the Te weight is in the CB, which is quantitatively shown in Fig. 2(c). The Bi and Te p_z orbital weights switch at $d_{av} \sim 0.4$ Å with the Bi weight decreasing in the CB and the Te weight increasing (vice versa for the VB). Importantly, the average atomic displacement of 0.4 Å is observed in amorphous TI systems and so is a physically reasonable amount of disorder

that could be induced in amorphous materials [10]. This allows us to reasonably assume the electronic structure of the disordered crystal could reflect an amorphous phase. Additionally, the peak in the distribution of coordination numbers in the disordered structures moves from six to five exactly at the TPT, producing a new crystal field. A minimal tight binding model incorporating disorder reproduces our results (presented in the supplemental materials). The generality of this model capturing the TPT with disorder can be applied to other structurally disordered materials systems with strong SOC.

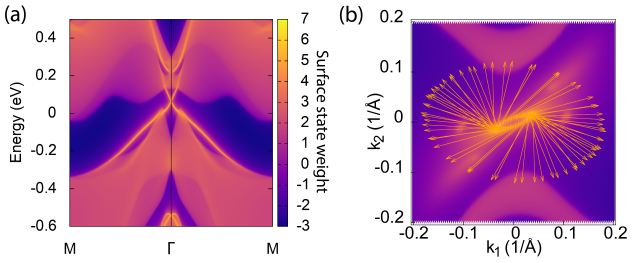

FIG. 3. **Calculated surface state spectrum for disordered BiTeI**. (a) The momentum dependent local density of states shows a topological Dirac cone around the surface Γ point. (b) The Fermi surface of the topological surface state. The Dirac cone is distorted due to the structural disorder, the resulting Fermi surface is stretched in k_x, k_y in momentum space, a result of the structural disorder in real space. Arrows correspond to the spin texture of the Fermi surface. Brighter colors represent a higher local density of states.

The electronic structure results are summarized in Fig. 2(d). We find the states at the Fermi level, namely Bi-p in the CB and Te/I-p in the VB, dominate the TPT. As previously noted, the in-plane C_{3v} rotational symmetry in crystalline BiTeI results in degenerate $p_{x,y}$ orbitals split in energy from the p_z orbital due to the semi-ionic polar trigonal prismatic coordination of the Bi [33]. This results in Bi-p_z and Te-p_z states at the edge of the CB and VB respectively [34], separated by a calculated band gap of 0.38 eV. Introducing disorder that shortens Bi-Te bonds results in greater orbital overlap between the Bi-p_z and Te-p_z states, pushing bands near the Fermi level closer together. This disorder-induced reduction in bandgap is then sufficient, once SOC is included, to cause a band inversion of the two opposite polarity bands, resulting in a TPT to a TI.

Since the TPT is that of an ordinary insulator to a TI in a noncentrosymmetric crystal upon structural disorder, we calculate the $\mathbb{Z}_2$ topological invariant for the TR-invariant planes in the BZ [23, 35]. After the TPT $\mathbb{Z}_2 = 1; (001)$ indicating a strong TI. Fig. 3(a) presents the surface state calculations performed on a slab of structurally disordered BiTeI after the TPT. The presence of a Dirac cone at the surface Γ confirms the nontrivial bulk $\mathbb{Z}_2$ invariant. The Dirac cone sits mid gap and passes through the top of the Rashba split VB as $\Gamma \rightarrow M$ before connecting to the VB at M. This complex surface spectrum allows for the interplay of bulk Rashba split bands with the topological surface state. We plot the spin-momentum locking of the surface states with $H \propto \sigma \times \boldsymbol{k}$ in Fig. 3(b). The annular structure is distorted in momentum space due to the structural disorder in real space. Increasing structural disorder produces a TPT leading to a strong TI with a spin-polarized Dirac cone.

The local structure and its disorder play a key role in the TPT. We generated several sets of disordered interpolations via our random displacement process, different from the set presented. In these, the bonds lengths develop different distributions leading to varying local chemical environments and orbital overlaps. In one set, the shortening of the Bi-Te bond brought the structures close to a TPT. In another set the charge redistribution to the Bi-Te bond was not present, but led to a very large Rashba splitting in the bulk [23]. These trivial electronic structures show not all disorders and subsequent local environments produces a TPT, highlighting the need for identifying key structural markers in TPTs. Our results demonstrate that structural disorder can generate both TPTs and colossal Rashba splitting in SOC materials making it a new tuning parameter for quantum properties in small gap semiconductors with large SOC.

Studying the influence of random structural disorder in SOC systems has implications for topological materials. We find that crystal-field engineering can be achieved with structural disorder as a new theoretical tuning parameter for topological phases. Furthermore, disorder can be employed to identify the physical origin of the TPT, making it also a marker for topological phases. This leads us to a systematic prescription for inducing TPT in material as follows: (i) identify the orbital character of the states near the Fermi level, (ii) add random atomic disorder to break the degeneracy of the states and distort along the corresponding orbital direction to reduce the gap, (iii) close the gap and cause a band inversion. By incorporating tight-binding models and topological markers [9, 36, 37], we can potentially discover many disordered and amorphous topological materials candidates. The topological phase local environment in BiTeI, probed in our study via random atomic disorder, could be realized in amorphous thin films grown via physical vapor deposition. Short range ordering coupled with the atomic displacement in disordered or amorphous BiTeI could potentially show a topological phase in experiment.

In conclusion, we show that by randomly introducing structural disorder a TPT from a normal insulator to TI is achieved. Disordered BiTeI shows a bulk band inversion at the A point in the BZ which manifests as a spin-polarized topological Dirac cone with a strong topological invariant. The physical mechanism for this is broken crystalline symmetries which produce a unique crystal-field environment that pushes the states near the Fermi level closer together, inducing a band inversion.

Our work is a step towards understanding topological matter from a local bonding perspective and has implications for topological states that cannot be classified using crystalline symmetry indicators. They suggest a route to discovering topological states in disordered and amorphous materials by identifying the local mechanisms (orbital inversions, etc.) which produce a TPT in the crystal in the presence of disorder. Our work provides a study of disorder induced TPT in a real solid state system with chemical specificity and bonding environments via first principles, a system which can be readily synthesized and manipulated in the lab. Such small-gap systems with strong SOC and well defined local environments, are promising systems to study the interplay of structural disorder, symmetry breaking, and topology.

This work was primarily funded by the U.S. Department of Energy, Office of Science, Office of Basic Energy Sciences, Materials Sciences and Engineering Division under Contract No. DE-AC02-05-CH11231 (High-Coherence Multilayer Superconducting Structures for Large Scale Qubit Integration and Photonic Transduction program (QISLBNL). Work at the Molecular Foundry was supported by the Office of Science, Office of Basic Energy Sciences, of the U.S. Department of Energy under Contract No. DE-AC02-05CH11231. This research used resources of the National Energy Research Scientific Computing Center (NERSC), a U.S. Department of Energy Office of Science User Facility operated under Contract No. DE-AC02-05CH11231. This work was partially supported by the U.S. Department of Energy, Office of Science, Office of Basic Energy Sciences, Materials Sciences and Engineering Division under Contract No. DE-AC02-05- CH11231 within the Nonequilibrium Magnetic Materials Program (MSMAG). P. C. is supported by the National Science Foundation Graduate Research Fellowship under Grant No. 1752814.

[1] T. Zhang, Y. Jiang, Z. Song, H. Huang, Y. He, Z. Fang, H. Weng, and C. Fang, Nature **566**, 475 (2019).
[2] M. G. Vergniory, L. Elcoro, C. Felser, N. Regnault, B. A. Bernevig, and Z. Wang, Nature Publishing Group **566**, 480 (2019).
[3] F. Tang, H. C. Po, A. Vishwanath, and X. Wan, Nature Publishing Group **566**, 486 (2019).
[4] H. Watanabe, H. C. Po, and A. Vishwanath, Science Advances **4**, eaat8685 (2018).
[5] B. Bradlyn, L. Elcoro, J. Cano, M. G. Vergniory, Z. Wang, C. Felser, M. I. Aroyo, and B. A. Bernevig, Nature **547**, 298 (2017).
[6] J. Kruthoff, J. de Boer, J. van Wezel, C. L. Kane, and R.-J. Slager, Physical Review X **7**, 041069 (2017).
[7] K. Choudhary, K. F. Garrity, and F. Tavazza, Scientific reports **9**, 1 (2019).
[8] J. D. Cain, A. Azizi, M. Conrad, S. M. Griffin, and A. Zettl, Proceedings of the National Academy of Sciences (2020), 10.1073/pnas.2015164117, https://www.pnas.org/content/early/2020/10/02/2015164117.full.pdf.
[9] D. Varjas, A. Lau, K. Pöyhönen, A. R. Akhmerov, D. I. Pikulin, and I. C. Fulga, Phys. Rev. Lett. **123**, 196401 (2019).
[10] P. Corbae, S. Ciocys, and et al., arXiv preprint arXiv:1910.13412 (2019).
[11] A. Agarwala and V. B. Shenoy, Phys. Rev. Lett. **118**, 236402 (2017).
[12] Q. Marsal, D. Varjas, and A. G. Grushin, Proceedings of the National Academy of Sciences **117**, 30260 (2020), https://www.pnas.org/content/117/48/30260.full.pdf.
[13] M. S. Bahramy, B.-J. Yang, R. Arita, and N. Nagaosa, Nature Communications **3**, 679 (2012).
[14] M. S. Bahramy, R. Arita, and N. Nagaosa, Phys. Rev. B **84**, 041202 (2011).
[15] V. Brousseau-Couture, G. Antonius, and M. Côté, Phys. Rev. Research **2**, 023185 (2020).
[16] B. Monserrat and A. Narayan, Phys. Rev. Research **1**, 033181 (2019).
[17] S. A. Mack, S. M. Griffin, and J. B. Neaton, Proceedings of the National Academy of Sciences **116**, 9197 (2019), https://www.pnas.org/content/116/19/9197.full.pdf.
[18] S. Zhang, M. Xie, B. Cai, H. Zhang, Y. Ma, Z. Chen, Z. Zhu, Z. Hu, and H. Zeng, Phys. Rev. B **93**, 245303 (2016).
[19] J. Li, R.-L. Chu, J. K. Jain, and S.-Q. Shen, Phys. Rev. Lett. **102**, 136806 (2009).
[20] C. W. Groth, M. Wimmer, A. R. Akhmerov, J. Tworzydło, and C. W. J. Beenakker, Phys. Rev. Lett. **103**, 196805 (2009).
[21] N. Mott and E. Davis, *Electronic Processes in Non-Crystalline Materials*, Oxford Classic Texts in the Physical Sciences (Oxford University Press, 1979).
[22] J. S. Lee, G. A. H. Schober, M. S. Bahramy, H. Murakawa, Y. Onose, R. Arita, N. Nagaosa, and Y. Tokura, Phys. Rev. Lett. **107**, 117401 (2011).
[23] See Supplemental Material at [URL will be inserted by publisher] for calculation details, discussion of the structure, WCC evolution, and Rashba/Weyl effects. All files related to a published paper are stored as a single deposit and assigned a Supplemental Material URL. This URL appears in the articles reference list. (2020).
[24] G. Kresse and J. Furthmüller, Phys. Rev. B **54**, 11169 (1996).
[25] G. Kresse and J. Hafner, Phys. Rev. B **48**, 13115 (1993).
[26] J. P. Perdew, K. Burke, and M. Ernzerhof, Phys. Rev. Lett. **77**, 3865 (1996).
[27] A. A. Mostofi, J. R. Yates, G. Pizzi, Y.-S. Lee, I. Souza, D. Vanderbilt, and N. Marzari, Computer Physics Communications **185**, 2309 (2014).
[28] Q. Wu, S. Zhang, H.-F. Song, M. Troyer, and A. A. Soluyanov, Computer Physics Communications **224**, 405 (2018).
[29] K. Ishizaka, M. S. Bahramy, H. Murakawa, M. Sakano, T. Shimojima, T. Sonobe, K. Koizumi, S. Shin, H. Miyahara, A. Kimura, K. Miyamoto, T. Okuda, H. Namatame, M. Taniguchi, R. Arita, N. Nagaosa, K. Kobayashi, Y. Murakami, R. Kumai, Y. Kaneko, Y. Onose, and Y. Tokura, Nature Materials **10**, 521 (2011).
[30] J. Liu and D. Vanderbilt, Phys. Rev. B **90**, 155316 (2014).

[31] L. Petersen and P. Hedegrd, Surface Science **459**, 49 (2000).
[32] E. I. Rashba, Sov. Phys. Solid State **2**, 11091122 (1960).
[33] K. Ishizaka and et. al, Nature Materials **10**, 521 (2011).
[34] H. Zhang, C.-X. Liu, X.-L. Qi, X. Dai, Z. Fang, and S.-C. Zhang, Nature Physics **5**, 438 (2009).
[35] A. A. Soluyanov and D. Vanderbilt, Phys. Rev. B **83**, 235401 (2011).
[36] D. Varjas, M. Fruchart, A. R. Akhmerov, and P. M. Perez-Piskunow, Phys. Rev. Research **2**, 013229 (2020).
[37] Q. Marsal, D. Varjas, and A. Grushin, arXiv:2003.13701 .